Research Square

Preprints are preliminary reports that have not undergone peer review.
They should not be considered conclusive, used to inform clinical practice,
or referenced by the media as validated information.

Dual-Electrode Configuration for Enhanced Plasma Activated Water Production: Optimizing RONS Generation and Energy Efficiency

Haiying Chen

chenhaiying@jiangnan.edu.cn

Jiangnan University

Xiang Wu

Jiangnan University

Min Zhou

Jiangnan University

Tao Wang

Jiangnan University

Lingjun Wei

Jiangnan University

Research Article

Keywords: Plasma activated water, Dual-electrode configuration, Reactive oxygen and nitrogen species (RONS), Energy efficiency, Process optimization

Posted Date: September 4th, 2025

DOI: https://doi.org/10.21203/rs.3.rs-7422801/v1

License: This work is licensed under a Creative Commons Attribution 4.0 International License.
Read Full License

Additional Declarations:
No competing interests reported.

Tables 1 to 3 are available in the Supplementary Files section.

Dual-Electrode Configuration for Enhanced Plasma Activated Water Production: Optimizing RONS Generation and Energy Efficiency

Haiying Chen[1*], Xiang Wu[1], Min Zhou,Tao Wang, Lingjun Wei

Key Laboratory of Advanced Food Manufacturing Equipment Technology in Jiangsu Province, School of Mechanical Engineering, Jiangnan University, Wuxi Jiangsu 214122, China.

Contact details of the corresponding author:

Name: Associate Prof. Haiying Chen,

E-mail address: chenhaiying@jiangnan.edu.cn

Full postal address: Jiangnan University, 1800 Lihu Avenue, Wuxi, Jiangsu, 214122, China.

[1] These authors contributed equally.

Abstract: The production of plasma activated water (PAW) enriched with reactive oxygen and nitrogen species (RONS) is a prerequisite for high-efficient application of PAW in chemical fields. To address the limitations of conventional single-electrode PAW systems, this study innovatively designs a dual-electrode structure consisting of an upper - liquid electrode and a submerged electrode to effectively compensate for the low mass - transfer efficiency of the upper - liquid discharge mode and the instability of the products in the under - liquid discharge mode, thereby improving the discharge stability. The upper - liquid electrode adopts a four - needle T - shaped structure to adapt to the turbulent liquid surface, while the submerged electrode is covered in a quartz tube to ensure stable plasma discharge. Optimized at 171 V (input voltage), 0.019 mol/L NaCl, and 30 min, the system achieves nonlinear RONS generation (172.11, 5.11, 3.25 and 0.81 μmol/L for NO_2^-, NO_3^-, H_2O_2, and O_3, respectively). The total energy consumption is 145.9 J, and the energy efficiency reaches 10.74 $g/(KW\times h)$. The device performance of the PAW generator is satisfactory, with temperature fluctuations confined to 7.67–8.33 $°C$, a final pH of 3.07, and a production volume of 2.4 L out of a rated capacity of 3 L. These results underscore the potential of this design to establish a foundation for highly effective, low-energy PAW production across industrial applications.

Keywords: Plasma activated water; Dual-electrode configuration; Reactive oxygen and nitrogen species (RONS); Energy efficiency; Process optimization.

1 Introduction

Plasma-activated water (PAW), produced through atmospheric pressure plasma, has shown remarkable efficacy in bacterial inactivation and growth suppression, making it highly suitable for applications in biomedical fields[1, 2], food sterilization [3], and agricultural modification[4, 5]. The growing interest in PAW stems from its ability to generate various reactive oxygen and nitrogen species (RONS) through plasma–liquid interactions, making it an environmentally friendly alternative to traditional chemical treatments[6]. The concentration of RONS in PAW is a critical determinant of its sterilization efficacy. Reactive oxygen species (ROS), such as H_2O_2, $OH\cdot$, and O_3, are capable of oxidatively disrupting bacterial cell walls and membranes, leading to cellular inactivation[7-9]. Similarly, reactive nitrogen species (RNS), such as NO_2^-, NO_3^- and $ONOOH$, contribute to bacterial inactivation by lowering the pH of the solution, creating an acidic environment unfavorable for microbial growth[5]. Therefore, increasing the concentration of RONS is essential for enhancing the sterilization effectiveness of PAW.

At present, the generation of PAW typically involves various plasma discharge configurations, including Atmospheric Pressure Plasma Jet (APPJ), Dielectric Barrier Discharge (DBD), Gliding Arc Discharge, Pulsed Corona Discharge and Pin-to-Liquid systems[10]. Considering the ease of use and the ability to generate RONS in PAW, the most commonly utilized configurations focus on the following two systems. The first one employs gas-phase discharge techniques, such as DBD[11, 12] and APPJ[13, 14], to generate reactive species at the liquid surface. These species subsequently transfer into the water through gas–liquid mass transfer and the desired RONS are formed through a series of chemical reactions in the solution. However, the low efficiency of gas–liquid mass transfer and the instability of reactive species in aqueous environments significantly restrict their practical application efficiency[14, 15]. The second approach involves implementing direct discharge within the liquid medium, where various forms of internal discharge can generate different types and concentrations of RONS. This method could enhance the mass transfer efficiency of active particles to some extent.

MEDVECKÁ et al. (2022)[4] demonstrated that the application of corona discharge inside a liquid resulted in significantly higher H_2O_2 concentrations than surface discharge at the gas/liquid interface. However, this method yielded very low concentrations of NO_2^- and NO_3^-, which led to an increase in the pH of the liquid and subsequently diminished the sterilization effectiveness. Wong et al., (2023)[16] clarified that adjusting the distance between the plasma jet and the liquid surface only affected the concentration of H_2O_2, with little impact on RNS species. Dhaliwal et al., (2024)[17] discovered that when the PAW generator was placed under the liquid for discharge, the concentrations of all RONS decreased to relatively low levels. Therefore, neither of these primary methods could produce PAW with high concentrations and multiple reactive species simultaneously. This limitation underscored the importance and urgency of seeking a method to substantially enhance the generation of RONS, presenting a compelling practical challenge.

Energy efficiency in PAW generation has become a critical focus area, with researchers exploring various strategies to optimize the process. The use of dual-electrode configurations has shown promise in enhancing plasma stability and increasing reactive species production[18]. Additionally, the introduction of turbulence in the liquid phase has been found to improve mass transfer and reaction kinetics[19]. Man et al., (2022)[20] indicated that the introduction of bubbles could significantly enhance both the concentration of RONS and the production efficiency. Rathore et al., (2023)[21] further confirmed that PAW systems equipped with bubble generators performed in a turbulent liquid state and resulted in an improved RONS concentration. Moreover, compared with stirring-induced turbulence, bubble-induced turbulence more effectively increased the concentration of reactive species. However, it was also observed that the microbubbles induced only localized liquid fluctuations within the container and failed to fully exploit their potential in enhancing the mass transfer of active particles through changes in liquid dynamics[22]. A close correlation might exist between bubble size and its impact on PAW production efficiency. Despite these advances, more efficient and scalable PAW generation systems are needed. The optimization of process parameters and the development of novel electrode

configurations were essential for improving PAW production efficiency[23]. Furthermore, the relationship between operational parameters and PAW properties needed to be better understood to enable precise control of PAW characteristics for specific applications.

This study aimed to design a novel dual - electrode coupled PAW generator to address the issue of insufficient concentrations of RONS in PAW. The system combined the characteristics of enhanced turbulence and dual - electrode hybrid discharge to effectively promote the generation, diffusion, and dissolution of reactive species, thus significantly increasing the yield of RONS. Response surface methodology (RSM) was employed to optimize key operational parameters influencing the generation efficiency and characteristics of PAW. The synergistic combination of the dual-electrode design and optimized parameters was anticipated to amplify bubble size to the centimeter scale and enhance PAW production capacity, laying a certain foundation for the industrialization of PAW production.

2 Materials and methods

2.1 Chemicals and materials

The reagents used in this study are as follows: sulfonamide (AR, Suzhou Great Pharmaceutical Technology Co., Ltd., China); N-(1-naphthyl) ethylenediamine, dihydrochloride (AR, Sinopharm Chemical Reagent Co., Ltd., China); disodium hydrogen phosphate (CP, Shanghai Macklin Biochemical Technology Co., Ltd., China); sodium indigo disulfonate (AR, Shanghai Merrier Biochemical Technology Co., Ltd., China); phosphoric acid, sodium nitrite and lithium nitrate (AR, Shanghai Titan Scientific Co., Ltd., China).

2.2 Dual-electrode coupled PAW generation system

The PAW generation system used in this study was a self-designed apparatus as depicted in Fig.1, comprising a high-voltage alternating current power supply (1) (CTP-2000 K, Nanjing Suman Plasma Technology Co., Ltd., China), a plasma-activated water generator (4), a gas valve (5) (AR 2000, Yangzhou Zhuohui Automation Equipment Co., Ltd., China) and an air compression pump (6) (OTS-550, Taizhou Outus Industry and

Trade Co., Ltd., China). Real-time monitoring of the voltage and current was performed and the results were recorded with an oscilloscope (2) (TDS3034C, Tektronix, USA). An air compressor was utilized to supply the gas necessary for plasma generation. The rated airflow of the compressor was 40 L/min, whereas the gas flow was regulated at 5 L/min through a gas valve.

The dual-electrode coupled PAW generator was composed of a large beaker (7), a self-designed insulating cover (8), a dual-electrode configuration with an upper liquid electrode (15) and a submerged electrode (13-14), and an additional electrode (12) for a unilateral discharge test. The beaker (7) was made of borosilicate glass, with a rated capacity of 3 L, and the volume of PAW prepared was 2.4 L every batch. The double electrodes (13-15) and the unilateral test electrode (12) were made of stainless steel, and the burrs on the surface were removed. The top of the beaker was covered with a self-designed insulating cover (8) made of polypropylene and polytetrafluoroethylene, which could effectively isolate the external environment and prevent gas leakage. Above the insulating cover, there were air outlets (9), air inlets (10) and water inlets and outlets (11) with diameters of 8, 8, and 12 mm, respectively, were used to control the flow of gas and liquid.

2.3 PAW generation process

The generation process of PAW using a dual-electrode configuration was outlined as below. First, 2.4 L of deionized water containing a certain concentration of NaCl was poured into a borosilicate glass beaker, connecting the high-voltage line to the submerged electrode (13-14) and the low-voltage line to the above-liquid electrode (15). Then, activate the air compressor (6) and adjust the gas flow rate to 5 L/min by using a gas valve (5). Next, switch on the high-voltage AC equipment (1), set the input voltage at 125/175/225 V, and fine-tune the output frequency knob. When plasma was generated at both electrodes, start timing immediately. Monitoring the temperature and pH values during the process every 5 min. When the preset time (10, 20, 30 min) was reached, turn off the power supply (1) and air compression pump (6). Afterward, the concentrations of RONS were determined immediately.

The generation process of PAW merely with a submerged electrode (13-14) was similar to that of PAW with dual-electrode. Only the low-voltage line needed to be connected to the unilateral test electrode (12).

2.4 Detection of RONS concentration of PAW

In this study, the types of RONS measured were NO_3^-, NO_2^-, H_2O_2, and O_3, respectively. The measurements relied mainly on ultraviolet spectrophotometry (UV-1800, Shimadzu Corporation, Japan) and related chemical reagents. The specific measurement methods were as follows.

NO_3^-: The concentration of NO_3^- was measured via the methods described by Zhang et al., (2024)[24] and Rathore et al., (2021)[25] with slight modifications. First, the $LiNO_3$ standard solutions were prepared at concentrations of 0.2, 0.4, 0.6, 0.8, and 1.0 mg/L, respectively. The absorbance at each concentration was subsequently measured at a wavelength of 220 nm to plot a standard curve. Afterward, the sample solution was appropriately diluted, and its absorbance was measured via the same method. Finally, the concentration of NO_3^- in the sample was calculated on the basis of the established standard curve, and the dilution factor was considered.

NO_2^-: The concentration of NO_2^- was measured via the method described by Mustapha et al., (2024)[26] with slight modifications. First, prepare a color reagent capable of reacting with nitrite to form a pink azo dye, which exhibited peak absorbance at 540 nm. Dissolve 40 g of sulfanilamide in a mixture of 100 ml phosphoric acid and 500 ml water. Add 2 g of N-(1-naphthyl) ethylenediamine dihydrochloride, and dilute the solution to a total volume of 1000 ml. Subsequently, prepare $NaNO_2$ standard solutions at concentrations of 0.02, 0.05, 0.1, 0.15, and 0.2 mg/L, respectively, and react with the color reagent. Measure the absorbance at 540 nm to construct a standard curve. Afterward, the sample solution was appropriately diluted and its absorbance was measured using the same method. The nitrogen concentration in the sample was calculated on the basis of the standard curve and dilution factor, and then the concentration of NO_2^- in the sample was obtained by multiplying this value by a factor of 3.29.

H_2O_2: The hydrogen peroxide detection kit (Wuhu Jing Biological Technology Co.,

Ltd., China) was used for measurement. Immediately after the preparation of PAW, hydrogen peroxide was determined in accordance with the kit instructions, and its concentration was determined via the colorimetric method.

O_3: The concentration of O_3 was measured via the method described by Perinban et al., (2022)[27] with slight modifications. The indigo-phosphate reagent solution was prepared by dissolving 0.075 g of indigo disulfonate sodium and 0.2 ml of phosphate buffer solution in deionized water, followed by dilution to a final volume of 150 ml. Subsequently, 1.0 ml of this reagent and 5.0 ml of phosphoric acid buffer solution (pH 2.0) were added to both the sample solution and deionized water, and the absorbance was measured at a wavelength of 610 nm. The O_3 concentration in the sample solution was calculated via Equation (1).

$$\rho = \frac{(A_0 - A_1) \times 25 \times 10^6}{\varepsilon \times b \times 5} \times 0.048 \quad (1)$$

where, ρ was the mass concentration of ozone, mg/L; A_0 and A_1 were the absorbances of deionized water and sample solution after adding the indigo-phosphoric acid reagent, respectively; ε was the molar absorptivity of the sodium indigo disulfonate solution, $2\times10^4\ L/(mol \times cm)$; b was the thickness of the cuvette, 1 cm.

2.5 Real-time monitoring of temperature and pH

Real-time monitoring of the temperature and pH during the preparation process of PAW was conducted and recorded every 5 min using a thermometer (TM - 902 C, Xinghua Jiuzhou Electric Heating Instrument Co., Ltd, China) and a pH meter (CT - 6021 A, Shenzhen Kedia Electronics Co., Ltd, China), respectively.

2.6 Response surface optimization experimental method

In this study, the treatment time, input voltage and NaCl content (initial conductivity) were selected as independent variables, whereas the concentrations of NO_2^-, NO_3^-, H_2O_2 and O_3 were designated as response variables for the response surface experiments. Preliminary experiments were conducted to establish the experimental range of each factor, as detailed in Table 1. The experimental design was implemented using the Box-Behnken method in Design Expert software. To minimize

bias and mitigate other uncontrollable external sources of variation, the experiments were randomized. Each set of experiments was repeated three times, and the average values were recorded.

2.7 Multiresponse variable optimization method

Desirability function analysis was a method that enabled the transformation of multiresponse parameters into a single-response parameter[28, 29]. This approach aimed to establish uniform coordination of RONS concentrations, thereby ensuring that all RONS concentrations attained relatively high values. The specific steps were as follows:

Step 1: Calculate the individual desirability function using the Equation (2).

$$d_t(Y_t) = \begin{cases} 0, & Y_t < A_t \\ \left(\dfrac{Y_t - A_t}{U_t - A_t}\right), & A_t \le Y_t \le U_t \\ 1, & Y_t \ge U_t \end{cases} \quad (2)$$

where, $d_t(Y_t)$、Y_t、A_t and U_t represented the individual expected value, the response value, and the lower and upper limits of response variable t, respectively. The maximum and minimum values within the experimental data were identified to establish the upper and lower limits. The individual expected values of the four response variables were represented by $d_{H_2O_2}$、$d_{NO_2^-}$、$d_{NO_3^-}$ and d_{O_3} respectively. The closer the value approached 1, the more effective the outcome.

Step 2: Calculate the overall desirability using the Equation (3), where the weights of all types of RONS were the same.

$$D = \left[d_{H_2O_2} \times d_{NO_2^-} \times d_{NO_3^-} \times d_{O_3}\right]^{\frac{1}{4}} \quad (3)$$

where, $d_{H_2O_2}$、$d_{NO_2^-}$、$d_{NO_3^-}$ and d_{O_3} represented the individual desirability values of the four response variables, and D represented the overall composite desirability.

Step 3: Discover the optimal combinations of parameters and levels. A higher composite desirability indicated superior product quality. The D value was used for estimating the parameter effect and the optimum level of each controllable parameter.

2.8 Energy efficiency calculation

Energy efficiency was calculated following the method of Wang et al., (2018)[30] with slight modifications. The total concentration of RONS was quantified as the sum of the NO_2^-, NO_3^-, O_3 and H_2O_2 concentrations, expressed in mg/L. The energy efficiency for the generation of reactive species was calculated as the ratio of the total RONS concentration to the average discharge power.

Energy injection:

$$E = \int_{to}^{to+T} u(t) \times i(t)\, dt \tag{4}$$

Discharge power:

$$P = E \times f \tag{5}$$

Energy efficiency

$$EE = \frac{Total\ of\ RONS}{P \times t \times 1000} \tag{6}$$

where, E was the energy injection, J; u(t) was the discharge voltage in volts, V; i(t) was the discharge current in amperes, A; t was the time in seconds, s; P was the discharge power, W; f was the discharge frequency, HZ; EE was the energy efficiency, $g/(KW \times h)$; Total of RONS was the sum of the concentrations of NO_2^-, NO_3^-, O_3 and H_2O_2, mg/L.

2.9 Statistical analysis

All the data were reported as the means ± standard deviation from at least three independent experiments or measurements. One - way analysis of variance was carried out via SPSS Statistics software, followed by Duncan's multiple - range test. At the 95% confidence level ($p < 0.05$), the least significant difference was considered statistically significant. Graphs were plotted using Origin 8.0 software.

3 Results and discussion

3.1 Configuration and discharge state of the dual-electrode coupled PAW generator

In this study, a novel dual-electrode PAW generator device is designed, and the configuration details are illustrated in Fig 1b and 1c. The dual electrodes used are a submerged electrode (13-14) and an above-liquid electrode (15) respectively. The

submerged electrode is composed of a quartz tube (13) and an electrode (14). The electrode (14) is further divided into two sections: the upper section with a radius of 7.5 mm, and the lower section, with a radius of 8.25 mm. The surrounding component is a quartz tube with an outer radius of 8.5 mm. The above - liquid electrode (15) is also composed of two cylindrical sections: the upper section has a radius of 4 mm, and the lower section has a radius of 15 mm. Moreover, four needle - shaped electrodes are evenly distributed on the lower half. Each of these four needle - shaped electrodes is uniformly composed of a cylinder with a radius of 2.5 mm and a height of 8 mm, and a cone with a radius of 2.5 mm and a height of 4 mm.

When the PAW generator device was in operation, an IDT Motion Pro Y4-S1 high-speed camera was employed to capture the entire operational characteristics at a frame rate of 1000 fps, with the results presented in Fig. 2. Upon activation, air initially entered the system through the inlet (10). Within the narrow gap between the quartz tube (13) and electrode (14), the incoming air underwent ionization, resulting in plasma generation (Fig. 2e). The generated plasma was entrained by the airflow and encapsulated within large air bubbles, which were subsequently introduced into the liquid-phase reaction chamber. These centimeter-sized bubbles were abundantly formed in the liquid medium (Fig. 2a), inducing significant turbulence that effectively enhanced mass and energy transfer across the gas-liquid interface. This process promoted the sustained release and diffusion of plasma-generated reactive species into the aqueous phase (Fig 2b). As the bubbles ascended through the liquid, the reactive species contained within gradually dissolved into the surrounding medium. Concurrently, some larger bubbles ruptured during ascent, releasing numerous smaller secondary bubbles (Fig 2c). These secondary bubbles created localized agitation, further enhancing liquid mixing and facilitating more thorough release and distribution of reactive species. Fig 2c and 2d depict the surface agitation and internal flow dynamics of the chamber, respectively. These observations indicate that the entire reaction system maintained a highly turbulent state under bubble motion, providing favorable conditions for interactions between plasma-generated species and water.

As shown in Fig. 2c, during the PAW generation process, liquid surface

fluctuations may cause the needle electrode in the upper liquid region to contact the water surface, thereby interrupting plasma discharge. To mitigate this issue, four needle-shaped electrodes were specifically designed to enhance discharge stability and maintain a continuous needle-to-liquid discharge state (Fig 2f). The discharge characteristics of the PAW generator were illustrated in Fig 2e and 2f. Submerged electrodes (13–14) exhibited efficient dielectric barrier discharge (DBD) beneath the liquid surface, with localized "filamentous" discharge observed at the electrode base. In contrast, the above-liquid electrode operated in a stable, continuous needle-to-liquid discharge mode. This dual-electrode configuration ensured consistent discharge performance throughout the process. Under the synergistic effects of bubble dynamics and turbulence, the dissolution and reaction kinetics of reactive species in solution were significantly enhanced. These hydrodynamic conditions facilitated efficient PAW production by promoting mass transfer across the gas-liquid interface.

3.2 Device performance of the dual-electrode coupled PAW generator

3.2.1 RONS concentration

During PAW production, the generation of RONS represented a critical parameter for evaluating the performance of PAW device. To verify the superiority of the dual-electrode hybrid discharge configuration, the RONS generation capacity was compared between the dual-electrode configuration and a single submerged electrode. Key indicators included nitrite (NO_2^-), nitrate (NO_3^-), hydrogen peroxide (H_2O_2), and ozone (O_3). The PAW preparation parameters were set at 171 V, 0.019 % NaCl for 30 min, and the results were depicted in Fig. 3.

As shown in Fig. 3, the concentrations of NO_2^-, NO_3^-, H_2O_2 and O_3 produced through single submerged electrode discharge were 46.18±5.25, 3.73±0.16, 1.99±0.28 and 0.29±0.01 mg/L respectively. In the dual-electrode hybrid discharge mode, these concentrations increased to 172.11±12.85，5.11±0.07, 3.25±0.41 and 0.81±0.06 mg/L, which corresponded to respective enhancements of 272.71 %, 37.11 %, 63.86 % and 177 % as compared to the single-electrode configuration (Fig. 3). This phenomenon confirmed that simultaneous discharge above and below the liquid effectively enhanced the RONS concentrations, which aligned with the findings

reported in previous studies[16, 31, 32]. This enhanced performance was partly attributed to the bubble-assisted turbulence effect generated by the designed discharge structure during PAW production. When air was introduced into the liquid phase, ionized gas subsequently entered the liquid alongside with the bubbles. As the bubbles underwent shrinkage, the internal pressure increased. The existence of ion clouds both inside and outside the bubbles, coupled with abrupt fluctuations in bubble pressure and ion concentrations, further amplified this effect. Consequently, the transfer and dissolution of reactive species were markedly enhanced[33-35]. Bubble bursting induced mechanical agitation and localized heating at the rupture site. This phenomenon propagated rapidly through the surrounding liquid medium, facilitating chemical reactions and potentially generating additional active free radicals. This process might also contribute to the increased RONS concentration[36, 37]. Additionally, bubbles generated by the self-designed dual-electrode hybrid discharge configuration in this study attain centimeter-scale dimensions, inducing a turbulent state throughout the liquid and further accelerating particle diffusion. In regions characterized by turbulent inertia, particle collisions with the surrounding fluid occurred more frequently, thereby enhancing the mass transfer capacity of active particles[38]. Thereby, the performance of the PAW generator incorporating the dual-electrode hybrid discharge configuration is generally satisfactory.

3.2.2 Discharge characteristics

Discharge phenomena in liquids typically impose significant demands on the power supply. To improve energy efficiency and minimize the breakdown voltage, it is necessary to consider the impedance matching between the PAW generator and the power supply[20, 39]. As illustrated in Fig. 2e-2f, the generator can achieve a nearly ideal dielectric barrier discharge (DBD) mode beneath the liquid, as well as a needle-liquid discharge state that effectively accommodates turbulent liquids. Notably, both modes are enabled by a single power supply to achieve the desired outcomes.

Energy consumption is another crucial factor in evaluating the performance of PAW devices. The terminal voltage and current of the single - submerged - electrode discharge and dual - electrode hybrid discharge of the PAW generator were measured

via the P3010 probe and a Tektronix oscilloscope and the waveforms are presented in Fig. 4. The peak-to-peak voltage for dual-electrode hybrid discharge is 19 kV, with a frequency of 10 kHz. The discharge current varies periodically between -0.1 A and 0.1 A, remaining stable throughout the process. This results in an energy consumption of 145.89 J over a duration of 30 min. In contrast, the peak-to-peak voltage for single submerged electrode discharge is 18.6 kV, with a frequency of 10 kHz. The discharge current fluctuates between -0.037 A and 0.168 A, resulting in an energy consumption of 180.55 J over the same period. In addition, the energy efficiency of single submerged electrode discharge is 2.50 $g/(KW \times h)$. Surprisingly, the energy efficiency of dual-electrode hybrid discharge can achieve a remarkable value of 10.74 $g/(KW \times h)$, which is regarded as an excellent level. This finding aligns with the energy efficiency (10.37 $g/(KW \times h)$) of the nanosecond-pulsed microbubble plasma reactor reported by Man et al., (2022)[20]. Therefore, the stability of dual-electrode hybrid discharge is superior to that of single submerged electrode discharge, likely due to the stronger electric field it generates. This enhanced electric field, in turn, contributes to improve plasma stability and facilitates more consistent voltage and current throughout the discharge process.

3.2.3 Real-time monitoring of temperature fluctuations (ΔT) and pH

During the PAW generation process, the pH value serves as a significant indicator of RNS species formation, whereas temperature fluctuations play a critical role in determining the RONS concentration and energy efficiency[40, 41]. Thereby, the ΔT and pH values are real-time monitored under 171 V with 0.019 % NaCl for a duration of 30 min and the results are demonstrated in Fig. 5A.

Throughout the 30-min discharge period, the temperature change (ΔT) for both the single-submerged-electrode and dual-electrode hybrid discharges remain within the range of 0 - 8.33 $°C$, showing an approximately linear upward trend. For single-submerged-electrode discharge, ΔT significantly rises by 1 - 2 $°C$ every 5 min during 30 min discharge. Meanwhile, the dual-electrode hybrid discharge demonstrates a more stable temperature increment, maintaining approximately 1 $°C$ per 5 min during the

first 15 min process and leveling off at 20 min. This disparity might be related to the higher energy loss (34.66 J) observed in the single-submerged-electrode mode than in the dual-electrode hybrid discharge mode. This increased energy loss could reduce the energy utilization efficiency, consequently affecting the experimental outcomes. In addition, prolong discharge time to 30 min, the ΔT disparity between the two discharge modes gradually decreases and the final ΔT stabilizes at 7.67 $°C$ to 8.33 $°C$, which is lower than that reported in other studies[36, 42]. This stability of ΔT might be partially attributed to the introduction of NaCl, which enhances the solution conductivity. In this environment, the discharge current distribution becomes more uniform, thereby reducing localized heating. Furthermore, the liquid turbulence accelerates heat diffusion, effectively limiting overall heat accumulation. These factors have significant implications for enhancing the RONS concentration while minimizing energy loss.

Moreover, both the single-submerged-electrode discharge and the dual-electrode hybrid discharge reduce the pH value of the solutions (Fig. 5A). During the initial 10 min of discharge, the rate of decrease in the pH value for both discharge modes is relatively slow. To elucidate the underlying causes, the initial discharge images of the two discharge modes are recorded (Fig. 5B-C). Upon activation of the device, the submerged electrode could not immediately achieve an optimal discharge state immediately (Fig. 5C), and this condition had a notable effect on the pH value. After a discharge period of 30 min, the final pH values observed under the single-submerged-electrode discharge mode is 3.53 whereas that under the dual-electrode hybrid discharge mode is 3.07. A similar phenomenon was also observed in the device developed by Hadinoto K et al., (2023)[22] in which the pH value of the solution reached 3.16 after treatment for 30 min. This result clearly demonstrates that the hybrid discharge mode exerts a beneficial effect on reducing the pH value.

3.3 Optimization of the process parameters of the dual-electrode coupled PAW generator

The process parameters of the device utilized in this study are optimized through the response surface methodology and the desirability function approach. The concentrations of RONS are measured immediately following the experiments and the

results are summarized in Table 2. Among the generated RONS, NO_2^- exhibits the highest concentration, followed by O_3, whereas NO_3^- and H_2O_2 show the lowest concentrations. Furthermore, the final pH values after discharge range among 3.3±0.00 to 3.9±0.00, while the temperature fluctuations are observed between 2.5±0.41 and 11.5±0.41.

The regression model utilized in this study is developed through the stepwise regression method. The resulting regression equations, expressed in coded units, are presented in Equations (7-10) respectively, which illustrate the significant relationships between RONS and each of the contributing factors. In these equations, A, B, and C represent the voltage, NaCl content, and time, respectively.

$$NO_2^- = 172.11 + 46.57A + 25.58B + 24.92C + 6.56AB + 10.49AC + 10.49BC - 47.88A^2 - 45.26B^2 - 43.95C^2 \quad (7)$$

$$NO_3^- = 4.81 + 0.3712A + 0.25B + 1.4C + 0.08AB - 0.5175AC + 0.05BC - 0.2471A^2 - 0.7946B^2 - 0.6471C^2 \quad (8)$$

$$H_2O_2 = 1.93 - 0.2125A - 0.6B + 0.6625C - 0.125AB - 0.5AC - 0.175BC + 0.7083A^2 + 0.1833B^2 + 0.4583C^2 \quad (9)$$

$$O_3 = 0.7433 + 0.0775A - 0.005B + 0.1225C - 0.2025AB - 0.0225AC + 0.0175BC - 0.2154A^2 - 0.1004B^2 - 0.0604C^2 \quad (10)$$

The F test was used to evaluate the statistical significance of the model. The analysis of variance (ANOVA) results indicate that all four models are significant at the 95% confidence level (Table S1-4). The assumptions of ANOVA are also validated, revealing no significant lack of fit for any of the four models. Furthermore, the determination coefficient (R^2), adjustment R^2, and prediction R^2 of NO_2^-, NO_3^-, H_2O_2 and O_3 are (99.84 %; 99.57 %; 99.07 %), (99.39 %; 98.28 %; 94.67 %), (99.39 %; 98.29 %; 96.33 %), and (98.95 %; 97.06 %; 91.95 %) respectively. Therefore, these factors account for a substantial portion of the variance in the response variables. On the basis of the *F*-value from the quadratic regression, the influence factors ranked by significance (from largest to smallest) are as follows: for NO_2^- concentration, voltage (A) > NaCl content (B) > time (C); forNO_3^- and O_3 concentration, time (C) > voltage (A) > NaCl content (B); for H_2O_2 concentration, time (C) > NaCl content (B) > voltage (A).

The optimized concentration results of RONS are summarized in Table 3 and the optimal conditions are an input voltage of 171.094 V, NaCl content of 0.018 %, and treatment time of 30 min. Under these conditions, the yields of NO_2^-, NO_3^-, H_2O_2 and O_3 are 143.03, 5.52, 3.22 and 0.80 mg/L respectively. The composite index calculation yields a desirability (D) value of 0.82, indicating a satisfactory optimization effect.

To validate the model's accuracy and simplify the operational procedures, the final preparation parameters are adjusted to: an input voltage of 171 V, NaCl content of 0.019 %, and treatment time of 30 min. Experimental validation under these conditions reveals that the concentrations of NO_2^-, NO_3^-, H_2O_2 and O_3 are 172.11 $\pm$ 12.85, 5.11 $\pm$ 0.07, 3.25 $\pm$ 0.41 and 0.81 $\pm$ 0.06 mg/L respectively (Table 3). These experimental results closely align with the simulation data, thereby verifying the reliability of the model.

3.4 Interaction effects among parameters on the RONS yield

3.4.1 NO_2^- concentrations

Contour plots and 3D surface diagrams depicting the interaction effects of the input voltage, NaCl content, and treatment time on the NO_2^- concentration are shown in Fig. 6. These visualizations reveal that the interactive effects of these factors exhibit significantly nonlinear influences on NO_2^- concentration, exhibiting a unimodal trend where concentrations initially increase and subsequently decrease with increasing factor levels. In particular, the interactive effect between treatment time and NaCl content is most pronounced, aligning with the earlier factor ranking (voltage > NaCl content > time) while highlighting their synergistic contribution to NO_2^- generation.

According to Table 2 and Fig. 6, the NO_2^- concentration gradually increases from 19.94 $\pm$ 4.28 mg/L to 172.11±3.80 mg/L with elevating voltage from 125 to 175 V, and extending treatment time from 10 to 20 min. This phenomenon can be attributed to enhanced air ionization at higher voltages, generating more reactive particles, while prolonged treatment time provides sufficient opportunity for these particles to dissolve into the solution. Conversely, when the input voltage and treatment time reach 225 V

and 30 min respectively, the NO_2^- concentration slightly decreases to 161.61±1.06 mg/L. Combined with the temperature fluctuation data during the PAW process (Table 2), this reduction might be attributed to the temperature increment of 7.5±0.41℃ to 9.5±0.41 $°C$. Studies indicate that gas-liquid temperature differentials influence the diffusion and dissolution rates of gaseous substances[20, 43, 44]. During air ionization, reactive particles are introduced into the solution through bubbles, resulting in a mixed aerosol formation. Notably, bubble temperature does not instantaneously equilibrate with water temperature, reducing gaseous solubility. Furthermore, considering the poor stability of NO_2^-, an increased solution temperature accelerates the reactions outlined in Chemical Reaction Equations (1-3) , thereby decreasing the NO_2^- concentration[41, 45, 46].

$$3NO_2^- + 3H^+ \rightarrow 2NO^- + NO_3^- + 3H^+ \quad (1)$$

$$NO_2^- + H_2O_2 + H^+ \rightarrow HOONO + H_2O \rightarrow NO_3^- + H^+ + H_2O \quad (2)$$

$$NO_2^- + O_3 \rightarrow NO_3^- + O_2 \quad (3)$$

When 0.021 % NaCl is introduced into the system, the concentration of NO_2^- is generally enhanced. This phenomenon might be ascribed to the increased initial conductivity of the solution upon NaCl addition, which enhances the electric field strength and discharge current at the gas-liquid interface, thereby promoting reactive species formation. Furthermore, plasma interaction with NaCl solution generates elevated levels of $^1O_2$ as indicated in Chemical Reaction Equations (4-12)[47-49]. These $^1O_2$ subsequently react with NO to form the short-lived reactive species $ONOOH$, which further decomposes into NO_2^- and $OH^- or NO_2^-$ and H^+ as reported in Kučerová K et al., (2020)[50]. However, when the NaCl concentration reaches 0.042%, a noticeable decreasing tendency in NO_2^- concentration occurs. This observation might be attributed to the low pH environment (pH 3.3±0.00 to 3.9±0.00) (Table 2) resulting from the significant increase in NO_2^- production during the early PAW generation stages. Under such acidic conditions, some Cl^- and HClO would interact with NO_2^-, leading to a reduction in the overall NO_2^- concentration[51, 52].

$$Cl^- + O \rightarrow ClO^- \quad (4)$$

$$Cl^- + O_3 \rightarrow ClO^- + O_2 \quad (5)$$

$$Cl^- + 2 \cdot OH \rightarrow ClO^- + H_2O \quad (6)$$

$$Cl^- + H_2O_2 \rightarrow ClO^- + H_2O \quad (7)$$

$$ClO^- + H_2O_2 \rightarrow Cl^- + H_2O + O_2 \quad (8)$$

$$\cdot OH + Cl^- \rightarrow HOCl^{\cdot -} \quad (9)$$

$$HOCl^{\cdot -} \rightarrow OH^- + Cl^{\cdot} \quad (10)$$

$$Cl^{\cdot} + Cl^- \rightarrow Cl_2^{\cdot -} \quad (11)$$

$$Cl_2^{\cdot -} + H_2O_2 \rightarrow 2Cl^- + 1O_2^{\cdot} + 2H^+ \quad (12)$$

3.4.2 NO_3^- concentrations

Contour plots and 3D surface diagrams depicting the interaction effects of the input voltage, NaCl content, and treatment time on the NO_3^- concentration are presented in Fig. 7. Similar to the NO_2^- concentration, these visualizations reveal that the interactive effects of these factors on the NO_3^- concentration are also nonlinear, with particularly pronounced interactive effects observed between the treatment time and voltage.

Combined with the results in Table 2 and Fig. 7, it is evident that the NO_3^- concentration is significantly lower than the NO_2^- concentration. Notably, the NO_3^- concentration gradually increases from 1.73 ± 0.03 to 5.52 ± 0.028 mg/L with extending treatment time from 10 to 30 min. Increasing the input voltage also results in a significant rise in NO_3^- concentration. At the same time, NO_3^- concentration exhibits an upward trend when the NaCl concentration gradually increases to 0.021 %. This might be associated with the mitigation of temperature fluctuations during the initial phase of PAW generation caused by NaCl addition. Conversely, further increasing the NaCl concentration to 0.042 % leads to a decrease in the NO_3^- concentration. This trend can be attributed to the interdependent formation pathways of NO_3^- and NO_2^- (Chemical Reaction Equations 13-18)[22, 41, 53]. In a low-pH environment, HClO and Cl^- may react with NO_2^- [51, 52], reducing NO_2^- availability. Since NO_3^- production partially relies on NO_2^- oxidation (Chemical Reaction Equations 16–17), the depletion of NO_2^- ultimately leads to a decline in the NO_3^- concentration.

$$2NO_{2aq} + H_2O \rightarrow NO_2^- + NO_3^- + 2H^+ \quad (13)$$

$$4NO_{2aq} + 2H_2O + O_{2aq} \rightarrow 4NO_3^- + 4H^+ \quad (14)$$

$$NO_{2aq} + OH_{aq} \rightarrow NO_3^- + H^+ \quad (15)$$

$$NO_2^- + H_2O_2 \rightarrow NO_3^- + H_2O \quad (16)$$

$$NO_2^- + O_{3aq} \rightarrow NO_3^- + O_{2aq} \quad (17)$$

$$3NO_2^- + 3H^+ \rightarrow 2NO^- + NO_3^- + 3H^+ \quad (18)$$

3.4.3 H_2O_2 concentrations

Contour plots and 3D surface diagrams depicting the interaction effects of the input voltage, NaCl content, and treatment time on the H_2O_2 concentration are presented in Fig. 8. Similar to the results for the NO_3^- concentration, these visualizations reveal that the interactive effects of these factors on the H_2O_2 concentration are also nonlinear, with particularly pronounced interactive effects observed between the treatment time and voltage.

As the treatment time increases, the concentration of H_2O_2 tendes to increase. This phenomenon is attributed primarily to the extended duration facilitating greater air electrolysis, which progressively enhances reactive particle production. These particles subsequently undergo sequential reactions to form H_2O_2 (Chemical Reaction Equations 19-32)[54, 55]. Furthermore, bubble-assisted turbulence technology enhances reactive particle solubility by increasing the gas-liquid interface contact area and residence time, providing optimal conditions for dissolution and further promoting H_2O_2 accumulation.

$$O + H_2O \rightarrow H + HO_2 \quad (19)$$

$$O_2 + H_2O \rightarrow OH + HO_2 \quad (20)$$

$$HO_2 + HO_2 \rightarrow H_2O_2 + O_2 \quad (21)$$

$$HO_2 + H_2O \rightarrow H_2O_2 + OH \quad (22)$$

$$H_2O + O_2 \rightarrow H_2O_2 + O \quad (23)$$

$$HO_2 + OH \rightarrow H_2O_2 + O \quad (24)$$

$$e^- + H_2O \rightarrow \cdot H + \cdot OH + e^- \quad (25)$$

$$e^- + O_2 \rightarrow O(3P) + O^1(D) + e^- \quad (26)$$

$$O^1(D) + H_2O \rightarrow 2 \cdot OH \quad (27)$$

$$e^- + N_2 \rightarrow N_2\left(A^3\sum\nolimits_U^+\right) + e^- \quad (28)$$

$$N_2\left(A^3\sum\nolimits_U^+\right) + H_2O \rightarrow \cdot OH + \cdot H + N_2 \quad (29)$$

$$UV + H_2O \rightarrow H_2O^* \quad (30)$$

$$UV + H_2O^* \rightarrow H^+ + OH^- \quad (31)$$

$$\cdot OH + \cdot OH \rightarrow H_2O_2 \quad (32)$$

As the input voltage increases, the concentration of H_2O_2 first decreases slightly and then rises gradually. This phenomenon might be ascribed to the fact that, although the generation rate of key free radicals responsible for H_2O_2 formation (such as $\cdot OH$) increases with higher voltage[55], some of these free radicals participate in competing reactions. For instance, Chemical Reaction Equations (33-38) illustrate interactions between free radicals and other reactive species[55, 56]. Nevertheless, as the voltage continues to increase, the overall generation rate of free radicals accelerates. Furthermore, bubble-assisted turbulence technology enhances the mass transfer efficiency of these radicals, thereby promoting their dissolution and subsequent conversion to H_2O_2, ultimately leading to a significant increase in the H_2O_2 concentration.

$$O_2 + e^- \rightarrow 2O \cdot + e^- \quad (33)$$

$$O_2 + O \cdot \rightarrow O_3 \quad (34)$$

$$OH \cdot + O_3 \rightarrow HO_2 \cdot + O_2 \quad (35)$$

$$O_3 + \cdot H \rightarrow \cdot OH + O_2 \quad (36)$$

$$O_3 + HO_2 \rightarrow \cdot OH + 2O_2 \quad (37)$$

$$\cdot OH + HNO_2 \rightarrow NO_2^{\cdot} + H_2O \quad (38)$$

As the NaCl content increases, the concentration of H_2O_2 is adversely affected, leading to its decomposition as demonstrated in Chemical Reaction Equations (39-41)[57]. With a further increase in NaCl concentration, the H_2O_2 concentration reaches a stabilization state. This phenomenon may be attributed to the positive correlation between the elevated initial conductivity and discharge intensity, which enhances the generation of reactive species of H_2O_2. Consequently, the hydrolysis process of H_2O_2 is gradually terminated, leading to a stabilization of its concentration.

$$H_2O_2 + Cl_2^- \rightarrow 2Cl^- + H^+ + HO_2 \quad (39)$$

$$H_2O_2 + Cl_2^- \rightarrow OH + OH^- + Cl_2 \quad (40)$$

$$Cl + H_2O_2 \rightarrow Cl^- + H^+ + HO_2 \quad (41)$$

3.4.4 O_3 concentrations

Contour plots and 3D surface diagrams depicting the interaction effects of the input voltage, NaCl content, and treatment time on the O_3 concentration are presented in Fig. 9. Similar to the results of the NO_2^- and NO_3^- concentrations, these visualizations reveal that the interactive effects of these factors on the O_3 concentration are also nonlinear, with particularly pronounced interactive effects observed between the NaCl content and voltage.

As shown in Table 2 and Fig. 9, the O_3 concentration increases gradually from 0.17±0.03 to 0.74±0.04 mg/L in response to both elevated voltage (125 - 175 V) and increased NaCl content (0 - 0.021 %). However, when the input voltage and NaCl content reach 225 V and 0.042 %, respectively, the O_3 concentration slightly decreases to 0.28 ± 0.02 mg/L. This decrease might be ascribed to the two following aspects. One is the reaction between Cl^- and O_3, as indicated in Chemical Reaction Equations (42-43)[57], directly reducing O_3 concentration. On the other hand, as the voltage continues to increase, the generation rate of free radicals such as $\cdot OH$ also rises. These free radicals subsequently react with O_3, as illustrated in Chemical Reaction Equations (34-37), leading to further decomposition of O_3. In addition, when prolong the treatment time, the O_3 concentration gradually rises and eventually approaches a stable state. This phenomenon may be attributed to the attainment of dynamic equilibrium between O_3 generation and decomposition rates, thereby facilitating concentration stabilization.

$$O_3 + Cl^- \rightarrow O_2 + ClO^- \quad (42)$$

$$O_3 + Cl_2^- \rightarrow ClO^- + Cl + O_2 \quad (43)$$

4 Conclusion

This study designed a novel dual-electrode PAW generator to enhance RONS production, with systematic optimization of key process parameters. The dual-electrode

configuration, integrating an upper-liquid electrode and a submerged electrode, enables centimeter-scale bubble amplification, improves discharge stability, and enhances turbulence, thereby promoting active particle diffusion and dissolution. This design addresses critical limitations of conventional single-electrode systems by mitigating the low mass-transfer efficiency of upper-liquid discharge and the product instability of submerged-liquid discharge. Under optimized conditions (171 V input voltage, 0.019% NaCl concentration, 30 min treatment time), the system achieved RONS concentrations of 172.11 ± 12.85 mg/L (NO_2^-), 5.11 ± 0.07 mg/L (NO_3^-, 3.25 ± 0.41 mg/L (H_2O_2) and 0.81 ± 0.06 mg/L (O_3), with a PAW production efficiency of 10.74 g/(KW × h). Notably, minimal thermal fluctuation (7.67 - 8.33 °C) and a final pH of 3.07 ensured process stability. Response surface methodology identified the treatment time as the dominant factor influencing NO_3^-, H_2O_2 and O_3, whereas the input voltage primarily affected NO_2^-. The NaCl concentration exhibited dual effects: low NaCl concentrations promoted RNS formation, whereas high NaCl concentrations inhibited RNS and suppressed ROS. These findings provide critical insights into high-efficiency PAW production and establish a theoretical foundation for industrial applications.

Credit authorship contribution statement

Haiying Chen: Conceived and designed the study, Participated in the planning, supervision and financing of the study. **Xiang Wu**: Carried out the experiments and analytical methods, Data curation, Writing-original draft. **Min Zhou**: Provided auxiliary support during the experiment. **Tao Wang**: Previous literature investigation and research work. **Lingjun Wei**: Writing-review and editing. All authors discussed the results and contributed to the final manuscript.

Declaration of competing interest

The authors declare that they have no known competing financial interests or personal relationships that could have appeared to influence the work reported in this paper.

Data availability

Data will be made available on request.

Acknowledgments

This research was financially supported by National Key Research and Development Program (2022YFD2100305).

Reference

[1] Kaushik, NK., Ghimire, B., Li, Y., Adhikari, M., Veerana, M., Kaushik, N., Jha, N., Adhikari, B., Lee, SJ., Masur, K., von Woedtke ,T., Weltmann KD., & Choi, EH. (2018). Biological and medical applications of plasma-activated media water and solutions. Biological chemistry, 400(1), 39-62. https://doi.org/10.1515/hsz-2018-0226

[2] Naeim, F. A., & Humud, H. R. (2023). Studying the Physicochemical Properties of Water Activated by Microwave-Induced Plasma Jet for Biological and Medical Applications. Acta Physica Polonica: A, 144(2), 81-86. https://doi.org/10.12693/APhysPolA.144.81

[3] Wang, Q Y., & Salvi, D. (2021). Recent progress in the application of plasma-activated water (PAW) for food decontamination. Current Opinion in Food Science, 42(Suppl C), 51-60. https://doi.org/10.1016/j.cofs.2021.04.012

[4] MEDVECKá, V., OMASTA, S., KLAS, M., MOOVSKá, S., KYZEK, S., & ZAHORANOVá, A. (2022). Plasma activated water prepared by different plasma sources: physicochemical properties and decontamination effect on lentils sprouts. Plasma Science and Technology, 24(1), 015503. https://doi.org/10.1088/2058-6272/ac3410

[5] Thirumdas, R., Kothakota, A., Annapure, U., Siliveru, K., Blundell, R., Gatt, R., & Valdramidis, V P. (2018). Plasma activated water (PAW): Chemistry, physico-chemical properties, applications in food and agriculture. Trends in Food Science & Technology, 77(0), 21-31. https://doi.org/10.1016/j.tifs.2018.05.007

[6] Shaji, M., Rabinovich, A., Surace, M., Sales, C., & Fridman, A. (2023). Physical Properties of Plasma-Activated Water. Plasma, 6(1), 45-57. https://doi.org/10.3390/plasma6010005

[7] Dolezalova, E., & Lukes, P. (2015). Membrane damage and active but nonculturable state in liquid cultures of Escherichia coli treated with an atmospheric pressure plasma jet. Bioelectrochemistry, 103(0), 7-14. https://doi.org/10.1016/j.bioelechem.2014.08.018

[8] Tian, Y., Ma, RN., Zhang, Q., Feng, HQ., Liang, YD., Zhang, J., & Fang, J. (2015). Assessment of the Physicochemical Properties and Biological Effects of Water Activated by Non-Thermal Plasma Above and Beneath the Water Surface. Plasma Processes & Polymers, 12(5), 439-449. https://doi.org/10.1002/ppap.201400082

[9] Yusupov, M., Bogaerts, A., Huygh, S., Snoeckx, R., Duin, A C. T. V., & Neyts, E C. (2013). Plasma-

Induced Destruction of Bacterial Cell Wall Components: A Reactive Molecular Dynamics Simulation. Journal of Physical Chemistry C, 117(11), 5993-5998. https://doi.org/10.1021/jp3128516

[10] Elena, C P., Adna, D., & Sylvain, C. (2020). Investigation of the Electrode Erosion in Pin-to-Liquid Discharges and Its Influence on Reactive Oxygen and Nitrogen Species in Plasma-Activated Water. Plasma Chemistry & Plasma Processing, 40(1), 145-167. https://doi.org/10.1007/s11090-019-10036-3

[11] Jin, Y S., Cho, C., Kim, D., Sohn, C H., Ha, C S., & Han, S T. (2020). Mass production of plasma activated water by an atmospheric pressure plasma. Japanese Journal of Applied Physics, 59(SH), SHHF05. https://doi.org/10.35848/1347-4065/ab7e13

[12] Thongsopa, C., Santalunai, S., Thosdeekoraphat, T., Kumkhong, S., Nakharuthai, C., Pasomboon, P., & Boonanuntanasarn, S. (2024). Optimisation of plasma-activated water: Plasma DBD technology and application in recirculating aquaculture system for Nile tilapia larval culture. Aquaculture, 591, 741049. https://doi.org/10.1016/j.aquaculture.2024.741049

[13] Ghimire, B., Szili, E J., Patenall, B L., Lamichhane, P., Gaur, N., Robson, A J., Trivedi, D., Thet, N T., Jenkins, A T A., Choi, E H., & Short, R D. (2021). Enhancement of hydrogen peroxide production from an atmospheric pressure argon plasma jet and implications to the antibacterial activity of plasma activated water. Plasma Sources Science and Technology, 30(3), 035009. https://doi.org/10.1088/1361-6595/abe0c9

[14] Qin, S., Wang, R., Li, H., Fan, K Y., Wang, G., & Zhang, Y Y. (2023). Study on the sterilization effect of plasma jet and plasma activated water on Streptococcus mutans. Journal of biomedical engineering, 40(3), 559-565. https://doi.org/10.7507/1001-5515.202212030

[15] Wang, QL., Xin, YB., & Sun, B. (2022). Characteristics of liquid-phase continuous arc discharge plasma. Plasma Processes & Polymers, 19(11), 1. https://doi.org/10.1002/ppap.202200046

[16] Wong, K S., Chew, N S. L., Low, M., & Tan, M K. (2023). Plasma-Activated Water: Physicochemical Properties, Generation Techniques, and Applications. Processes, 11(2213), 2213. https://doi.org/10.3390/pr11072213

[17] Dhaliwal, H K., Yang, X Q., & Roopesh, M. S. (2024). Continuous production and recirculation of plasma-activated water bubbles under different flow regimes for mixed-species bacterial biofilm inactivation inside pipelines. Journal of Food Safety, 44(3), e13128. https://doi.org/10.1111/jfs.13128

[18] Liu, K.,Yang, Z H., & Liu, S T. (2020). Study of the Characteristics of DC Multineedle-to-Water Plasma-Activated Water and Its Germination Inhibition Efficiency: The Effect of Discharge Mode and

Gas Flow. IEEE Transactions on Plasma Science, 48(4), 969-979. https://doi.org/10.1109/TPS.2020.2980040

[19] Meropoulis, S., & Aggelopoulos, C.A. (2023). Plasma microbubbles vs gas-liquid DBD energized by low-frequency high voltage nanopulses for pollutants degradation in water: Destruction mechanisms, composition of plasma-activated water and energy assessment. Journal of Environmental Chemical Engineering, 11(3), 109855. https://doi.org/10.1016/j.jece.2023.109855

[20] Man, C X., Zhang, C., Fang, H Q., Zhou, R W., Huang, B D., Xu, Y Z., Zhang, X X., & Shao, T. (2022). Nanosecond-pulsed microbubble plasma reactor for plasma-activated water generation and bacterial inactivation. Plasma Processes & Polymers, 19(6), 1-16. https://doi.org/10.1002/ppap.202200004

[21] Rathore, V., Jamnpara, N I., & Nema, S K. (2023). Enhancing the physicochemical properties and reactive species concentration of plasma activated water using an air bubble diffuser. Physics Letters. A, 482(0), 129035. https://doi.org/10.1016/j.physleta.2023.129035

[22] Hadinoto, K., Rao, N.R.H., Astorga, J B., Zhou, R W., Biazik, J., Zhang, T Q., Masood, H., Cullen, P J., Prescott, S., Henderson. R K., & Trujillo, F J. (2023). Hybrid plasma discharges for energy-efficient production of plasma-activated water. Chemical Engineering Journal, 451(Part 2), 138643. https://doi.org/10.1016/j.cej.2022.138643

[23] Gott, R P., Engeling, K W., Olson, J., & Franco, C. (2023). Plasma activated water: a study of gas type, electrode material, and power supply selection and the impact on the final frontier. Physical chemistry chemical physics : PCCP, 25(6), 5130-5145. https://doi.org/10.1039/d2cp03489a

[24] Zhang, H L., Wei, J., Xv, H J., Khan, I., Sun, Q X., Zhao, X H., Gao, J L., Liu, S C., & Wei, S. (2024). Bactericidal efficacy of plasma-activated water against Vibrio parahaemolyticus on Litopenaeus vannamei. Frontiers in Nutrition, 11, 1365282. https://doi.org/10.3389/fnut.2024.1365282

[25] Rathore, V., Pate,l D., Butani, S., & Nema, SK. (2021). Investigation of Physicochemical Properties of Plasma Activated Water and its Bactericidal Efficacy. Plasma Chemistry and Plasma Processing, 41(3), 871-902. https://doi.org/10.1007/s11090-021-10161-y

[26] Nasiru, M M., Boateng, E F., Umair, M., Alnadari, F., Bassey, A P., Qian, J., Yan, W J., Li, C Y., & Zhang, J H. (2024). Decontamination of egg-associated pathogens by plasma-activated water and hydrogen peroxide. Journal of Food Safety, 44(3), e13136. https://doi.org/10.1111/jfs.13136

[27] Perinban, S., Orsa,t V., Rie., Gariepy, Y., Lyew, D., & Raghavan, V. (2022). Evaluation of plasma-

activated water characteristics and its process optimization. Journal of Food Process Engineering, 45(11), 1-14. https://doi.org/10.1111/jfpe.14156

[28] Boyacı, A I., & Baynal, K. (2019). Optimisation of elastomeric bearings' vulcanisation process using response surface methodology and desirability function approach. Journal of Rubber Research, 22(4), 187-193. https://doi.org/10.1007/s42464-019-00027-6

[29] Vijayakumar, R., & Pannirselvam, N. (2022). Employing desirability function analysis for the multi-response optimisation of mild steel embossed plate shear connector using Taguchi technique. Sustainable Energy Technologies and Assessments, 54, 102863. https://doi.org/10.1016/j.seta.2022.102863

[30] Wang, H H., Wandell, R.J., Tachibana, K., Voráč, J., & Locke, B.R. (2019). The influence of liquid conductivity on electrical breakdown and hydrogen peroxide production in a nanosecond pulsed plasma discharge generated in a water-film plasma reactor. Journal of Physics D: Applied Physics, 52(7), 075201. https://doi.org/10.1088/1361-6463/aaf132

[31] Zhang, Y., Zhou, MH., & Lei, LC. (2007). Degradation of 4-chlorophenol in different gas-liquid electrical discharge reactors(Article). Chemical Engineering Journal, 132(1-3), 325-333. https://doi.org/10.1016/j.cej.2007.01.040

[32] Jiang, B., Zhengm JT., Qium S., Wu, MB., Zhang, QH., Yan, ZF., & Xue, QZ. (2014). Review on electrical discharge plasma technology for wastewater remediation, Chemical Engineering Journal 236(1), 348-368. https://doi.org/10.1016/j.cej.2013.09.090

[33] Hou, C Y., Lai, Y C., Hsiao, C P., Chen, S Y., Liu, C T., Wu, J S., & Lin, C M. (2021). Antibacterial activity and the physicochemical characteristics of plasma activated water on tomato surfaces. LWT - Food Science & Technology, 149, 111879. https://doi.org/10.1016/j.lwt.2021.111879

[34] Pan, J., Li, YL., Liu, CM., Tian, Y., Yu, S., Wang, KL., Zhang, J., & Fang, J. (2017). Investigation of Cold Atmospheric Plasma-Activated Water for the Dental Unit Waterline System Contamination and Safety Evaluation in Vitro. Plasma Chemistry and Plasma Processing, 37(4), 1091-1103. https://doi.org/10.1007/s11090-017-9811-0

[35] Zhou, RW., Zhou, RS., Wang, PY., Luang, BY., Zhang, XH., Fang, Z., Xian, YB., Lu, XP., Ostrikov, KK., & Bazaka, K. (2019).Microplasma Bubbles: Reactive Vehicles for Biofilm Dispersal. ACS Appl Mater Interfaces, 11(23), 20660-20669. https://doi.org/10.1021/acsami.9b03961

[36] Takahashi, M., Chiba, K., & Li, P. (2007). Free-Radical Generation from Collapsing Microbubbles in the Absence of a Dynamic Stimulus. The journal of physical chemistry, B. Condensed matter, materials,

surfaces, interfaces & biophysical, 111(6), 1343-1347. https://doi.org/10.1021/jp0669254

[37] Liu, YA., Zhang, H., Sun, JH., Liu, JX., Shen, X., Zhan, JX., Zhang, A., Ognie,r S., Cavadias, S., & Li P. (2018). Degradation of aniline in aqueous solution using non-thermal plasma generated in microbubbles, Chemical engineering journal, 345(1), 679-687. https://doi.org/10.1016/j.cej.2018.01.057

[38] Oehmke, T B., & Variano, E A. (2021). A new particle for measuring mass transfer in turbulence. Experiments in Fluids, 62(1), 1-10. https://doi.org/10.1007/s00348-020-03084-5

[39] Vanraes, P., & Bogaerts, A. (2018). Plasma physics of liquids—A focused review. Applied Physics Reviews, 5(3), 031103. https://doi.org/10.1063/1.5020511

[40] Fina, B L., Santamaría, B., Ferreyra, M G., Schierloh, L P., Chamorro, J C., Cejas, E., & Prevosto, L. (2024). Innovative application of plasma-activated water in the inactivation of Escherichia coli: Temperature-dependent chemical processes leading to the synergistic microbicidal effect. Food Control, 163, 110530. https://doi.org/10.1016/j.foodcont.2024.110530

[41] Zhou, ZY., Li, HY., Qi, ZH., & Liu, DP. (2024). Biological and Chemical Reactivities of Plasma-Activated Water Prepared at Different Temperatures. Plasma Chemistry and Plasma Processing, 44(1), 393-410. https://doi.org/10.1007/s11090-023-10379-y

[42] Abuzairi, T., Ramadhanty, S., Puspohadiningrum, D F., Ratnasari, A., Poespawati, N R., & Purnamaningsih, R W. (2018). Investigation on physicochemical properties of plasma-activated water for the application of medical device sterilization. AIP Conference Proceedings, 1933(1), 040017. https://doi.org/10.1063/1.5023987

[43] Staniec, A., Vlahos, P., & Monahan, E C. (2021). The role of sea spray in atmosphere–ocean gas exchange. Nature Geoscience, 14(8), 593-598. https://doi.org/10.1038/s41561-021-00796-z

[44] Kim, M., & Or, D. (2019). Microscale pH variations during drying of soils and desert biocrusts affect HONO and NH_3 emissions. Nature Communications, 10(1), 1-12. https://doi.org/10.1038/s41467-019-11956-6

[45] Pang, B L., Liu, Z J., Zhang, H Y., Wang, S T., Gao, Y T., Xu, D H., Liu, D X., & Kong, M G. (2022). Investigation of the chemical characteristics and anticancer effect of plasma-activated water: The effect of liquid temperature. Plasma Processes & Polymers, 19(1), 1-13. https://doi.org/10.1002/ppap.202100079

[46] Feizollahi, E., Basu, U., Fredua-Agyeman, R., Jeganathan, B., Tonoyan, L., Strelkov, S E., Vasanthan, T., Siraki, A G., & Roopesh, M S. (2023). Effect of Plasma-Activated Water Bubbles on

Fusarium graminearum, Deoxynivalenol, and Germination of Naturally Infected Barley during Steeping. Toxins, 15(2), 124. https://doi.org/10.3390/toxins15020124

[47] Hadinoto, K., Astorga, J B., Masood, H., Zhou, R W., Alam, D., Cullen, P J., Prescott, S., & Trujillo, F J. (2021). Efficacy optimization of plasma-activated water for food sanitization through two reactor design configurations. Innovative Food Science & Emerging Technologies, 74(Suppl C), 102867. https://doi.org/10.1016/j.ifset.2021.102867

[48] Haghighat, G., Sohrabi, .A., Shaibani, P M.,Van Neste, C.W., Naicker, S., & Thundat, T. (2017). The role of chloride ions in plasma-activated water treatment processes. Environmental Science-Water Research & Technology, 3(1), 156-168. https://doi.org/10.1039/C6EW00308G

[49] Jin, X L., Wang, X Y., Zhang, H M., Xia, Q., We,i D B., & Yue, J J. (2010). Influence of Solution conductivity on contact glow discharge electrolysis. Plasma Chemistry and Plasma Processing, 30(3), 429-436. https://doi.org/10.1007/s11090-010-9220-0

[50] Kučerová, K., Machala, Z., & Hensel, K. (2020). Transient Spark Discharge Generated in Various -N_2/O_2 Gas Mixtures: Reactive Species in the Gas and Water and Their Antibacterial Effects. Plasma Chemistry and Plasma Processing, 40(3), 749-773. https://doi.org/10.1007/s11090-020-10082-2

[51] Sebranek, J G., & JR, J B F. (1991). RATE OF NITRIC OXIDE FORMATION FROM NITRITE AS AFFECTED BY CHLORIDE ION CONCENTRATION. Journal of Muscle Foods, 2(1), 11-20. https://doi.org/10.1111/j.1745-4573.1991.tb00437.x

[52] Marcinkiewicz, J., Chain, B., Nowak, B., Grabowska, A., Bryniarski, K., & Baran, J. (2000). Antimicrobial and cytotoxic activity of hypochlorous acid: interactions with taurine and nitrite. Inflammation research, 49(6), 280-289. https://doi.org/10.1007/PL00000208

[53] Tachibana, K., & Nakamura, T. (2019). Comparative study of discharge schemes for production rates and ratios of reactive oxygen and nitrogen species in plasma activated water. Journal of Physics: D Applied Physics, 52(38), 1. https://doi.org/10.1088/1361-6463/ab2529

[54] Ghimire, B., Szili, E J., Patenall, B L., Lamichhane, P., Gau,r N., Robson, A J., Trivedi, D., Thet, N T., Jenkins, A. T A., Choi, E H., & Short, R D. (2021). Enhancement of hydrogen peroxide production from an atmospheric pressure argon plasma jet and implications to the antibacterial activity of plasma activated water. Plasma Sources Science and Technology, 30(3), 035009. https://doi.org/10.1088/1361-6595/abe0c9

[55] Liu, K., Liu, S T., & Ran, C F. (2020). The Effect of Air-Water-Plasma-Jet-Activated Water on

Penicillium The Reaction of HNO_2 and H_2O_2 Under Acidic Condition. Frontiers in Physics, 8. https://doi.org/10.3389/fphy.2020.00242

[56] Jiang, N., Li, X C., Li, J., Li, J., Liao, B., Peng, B F., & Liu, G. (2023). Pulsed gas–liquid discharge plasma catalytic degradation of bisphenol A over graphene/CdS: process parameters optimization and O3 activation mechanism analysis. Plasma Science and Technology, 25(10), 93-102. https://doi.org/10.1088/2058-6272/acbde5

[57] Liu, Z C., Guo, L., Liu, D X., Rong, M Z., Chen, H L., & Kong, M G. (2017). Chemical Kinetics and Reactive Species in Normal Saline Activated by a Surface Air Discharge. Plasma Process and Polymers, 14(4-5), 1600113. https://doi.org/10.1002/ppap.201600113

Figures

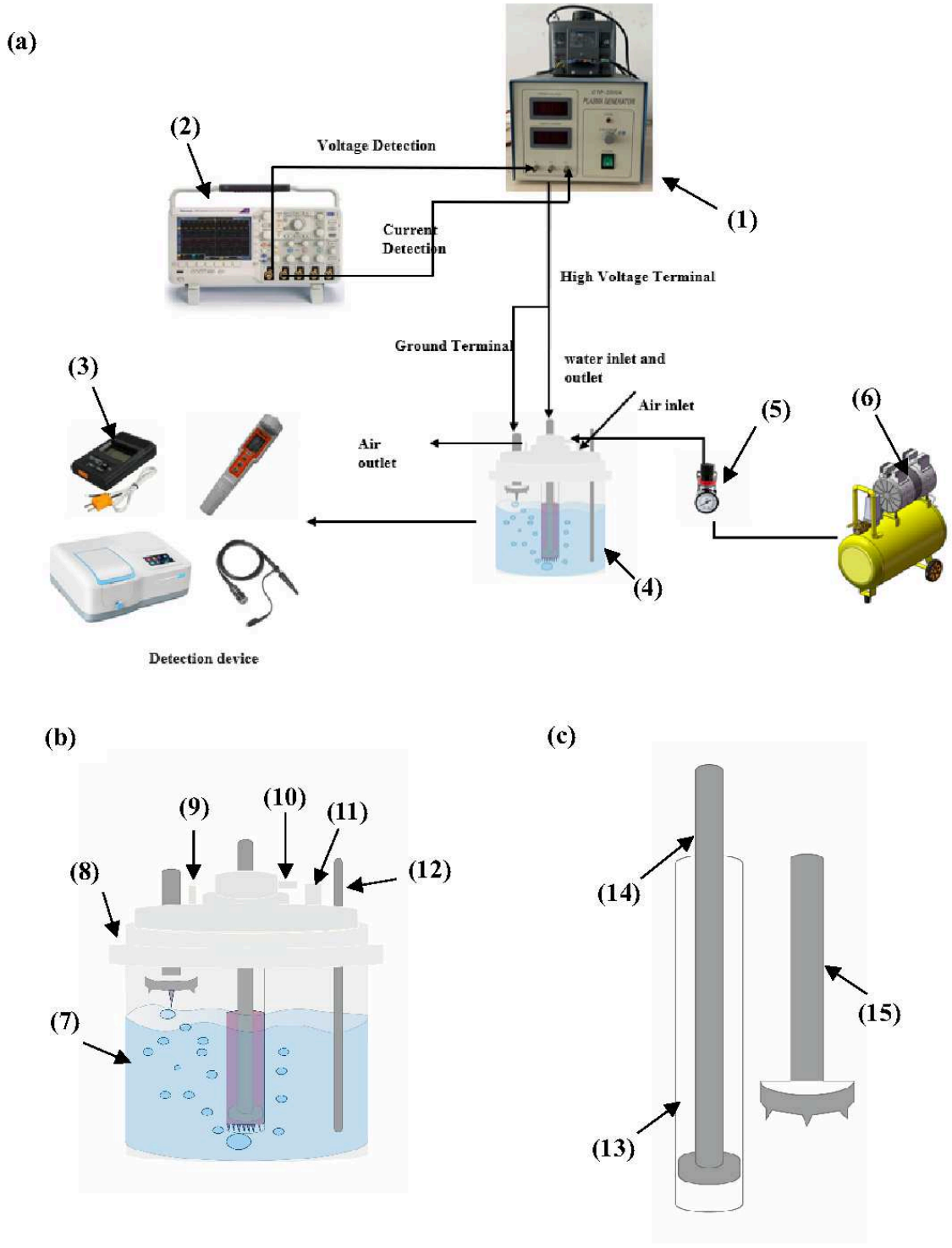


Figure 1

Plasma-activated water (PAW) generation system:

(a) PAW experimental device with High-voltage AC power supply and voltage regulator (1), Oscilloscope (2), Detection device (3), PAW generator (4), Gas valve (5), Air compressor (6);

(b) PAW generator with Large beaker (7), Insulation cover (8), Air outlet (9), Air inlet (10), Water inlet and outlet (11), Unilateral test electrode (12); Note:The purple tips under the electrode mean the discharge state.

(c) Electrode configuration with Submerged electrode (13–14), Above-liquid electrode (15).

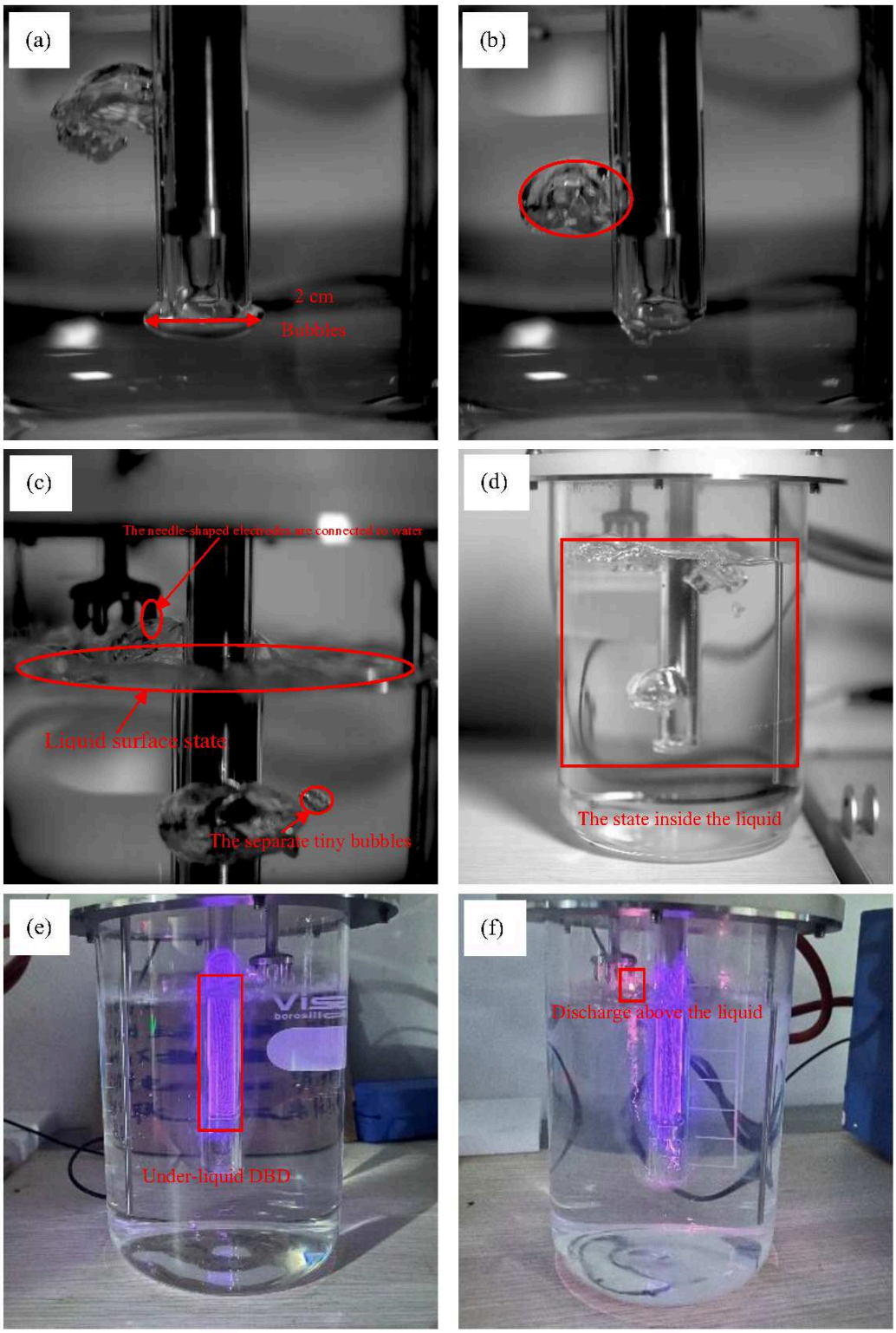


Figure 2

Dual-electrode hybrid discharge state diagram: (a-b) Bubble size; (c-d) Liquid state; (e-f) Discharge state of submerged electrode DBD and above-liquid electrode, respectively .

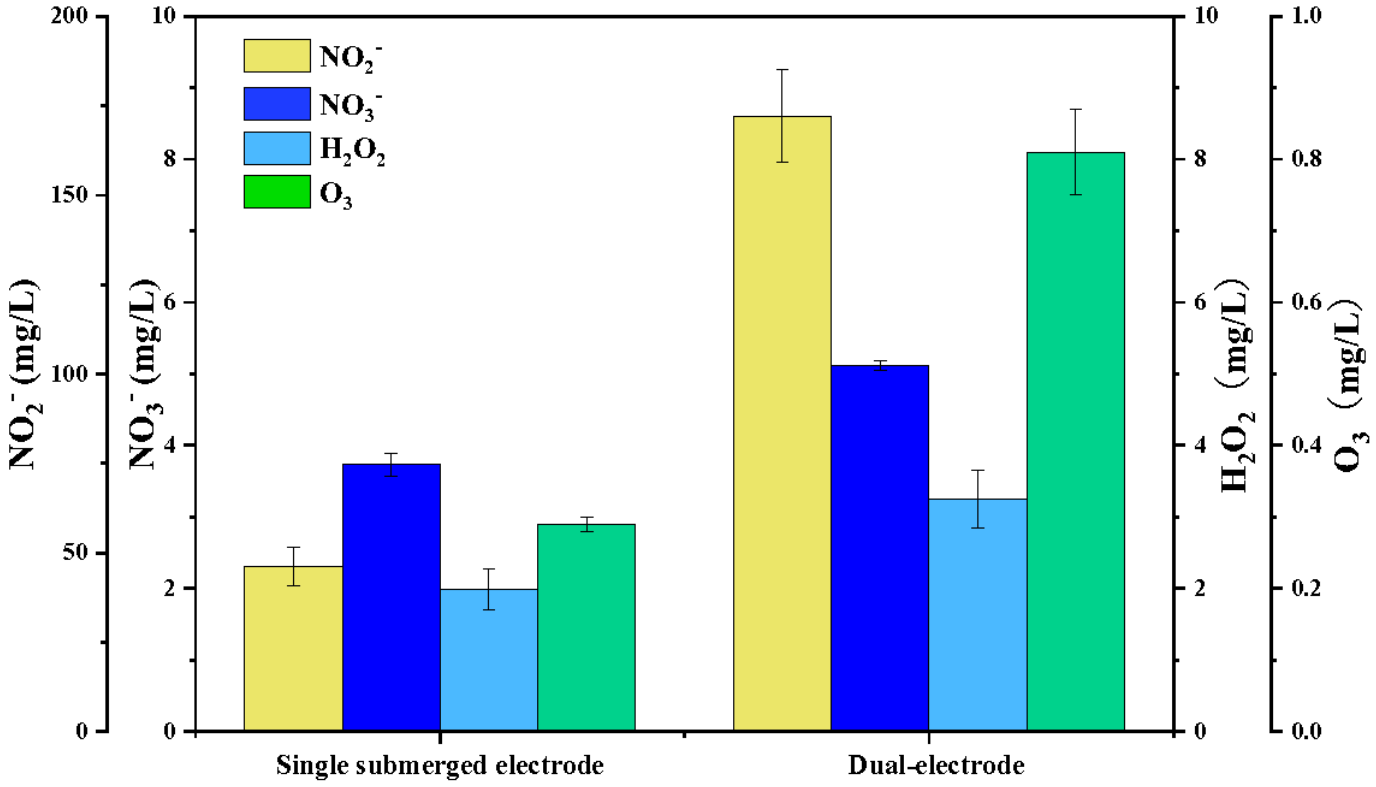


Figure 3

The RONS concentrations of PAW produced by single submerged electrode discharge and dual-electrode hybrid discharge under the same conditions respectively. All error bars represent the standard deviation.

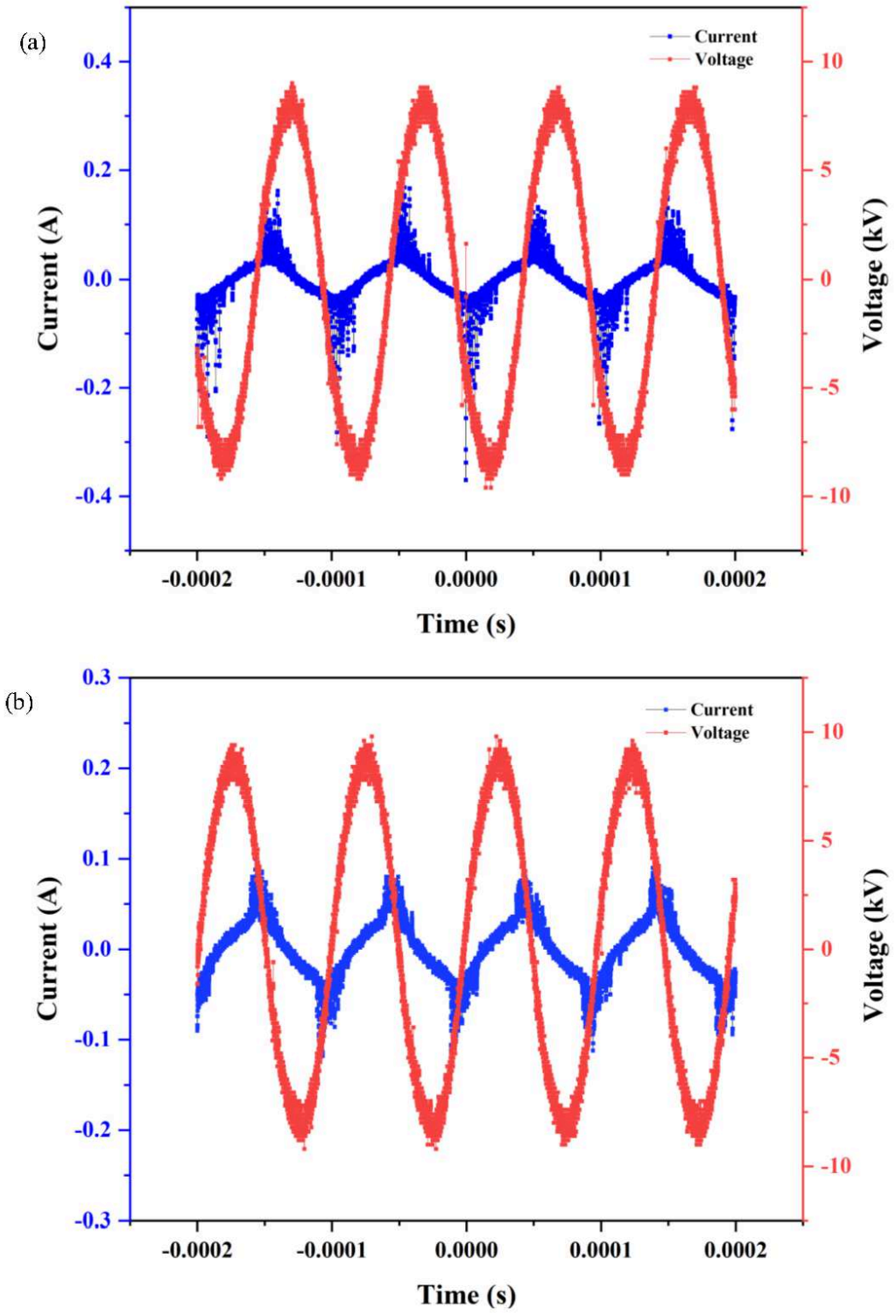


Figure 4

Voltage and current values of the PAW generator with single submerged electrode discharge (a) and dual-electrode hybrid discharge (b) under a high-voltage AC power supply.

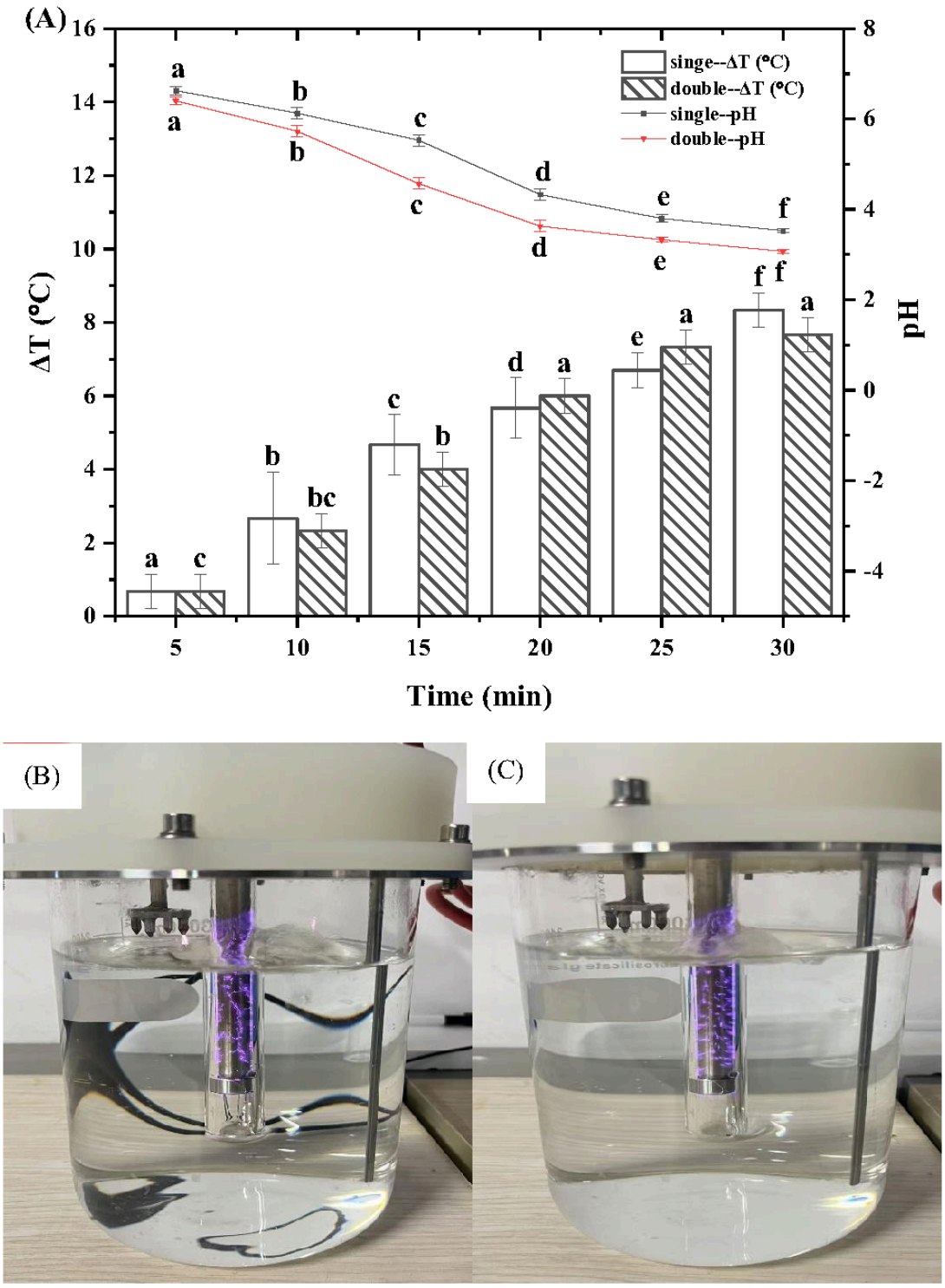


Figure 5

(A) The real-time monitoring of temperature and pH value during the dual-electrode hybrid discharge and single submerged electrode discharge;

(B-C) Initial discharge state of the dual-electrode hybrid discharge and the single-submerged-electrode discharge respectively.

Note: All error bars represent standard deviations. Under the same preparation conditions, different lowercase letters indicate significant differences ($p < 0.05$).

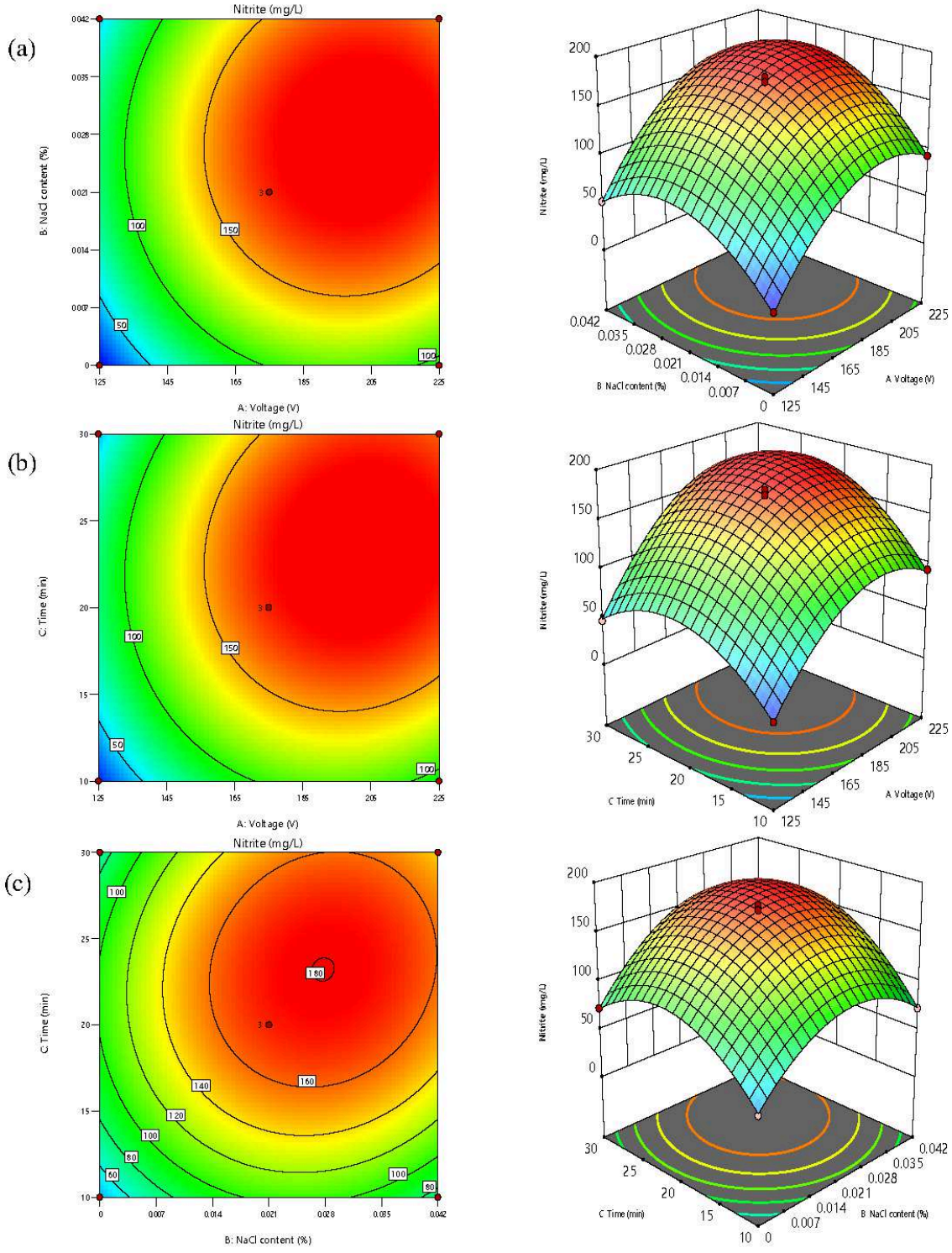


Figure 6

Interactive effects of input voltage, NaCl content and treatment time on NO^-_2 concentration: (a) input voltage and NaCl content, (b) input voltage and treatment time, (c) NaCl content and treatment time.

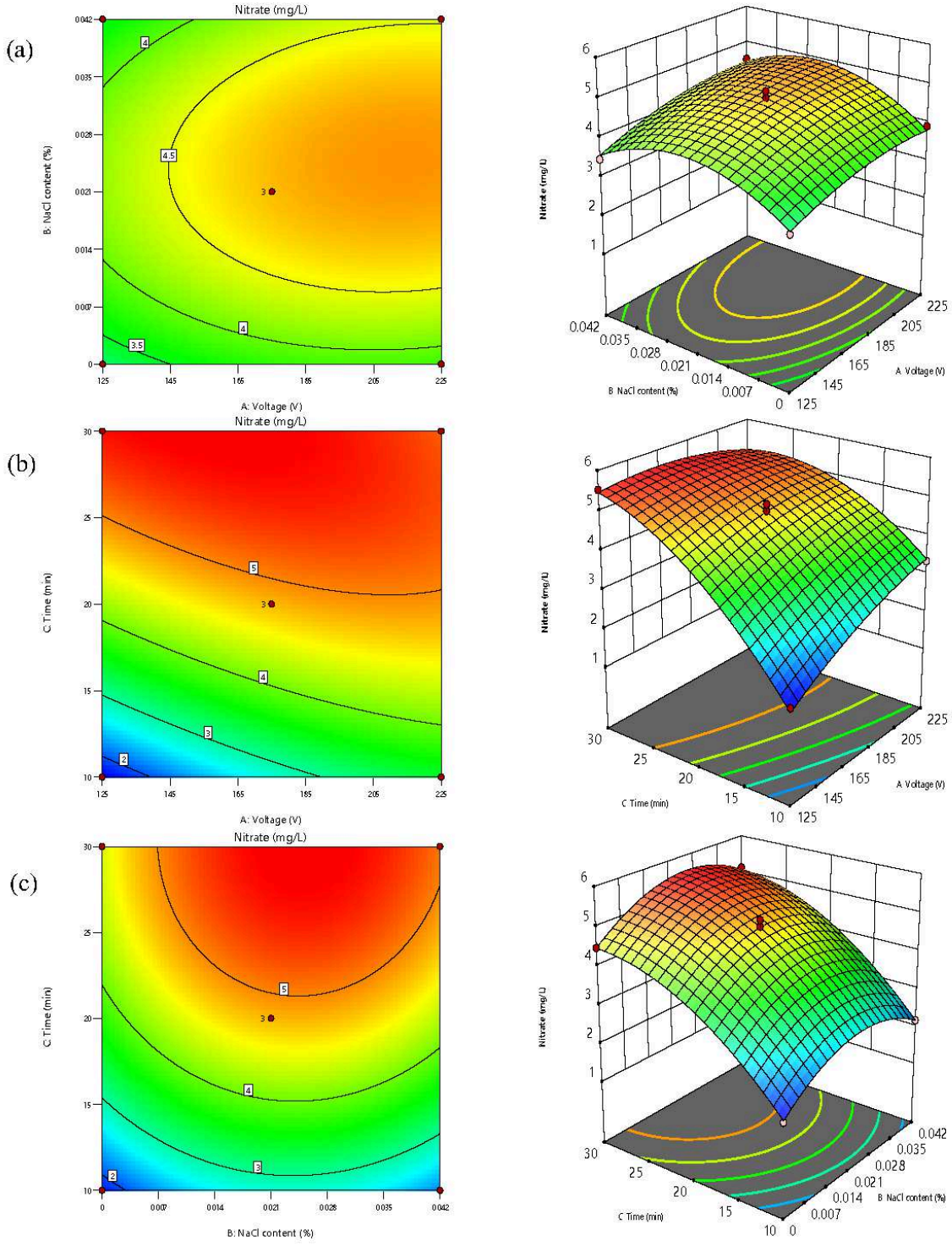


Figure 7

Interactive effects of input voltage, NaCl content, and treatment time on NO^{-}_{3} concentration: (a) input voltage and NaCl content, (b) input voltage and treatment time, (c) NaCl content and treatment time.

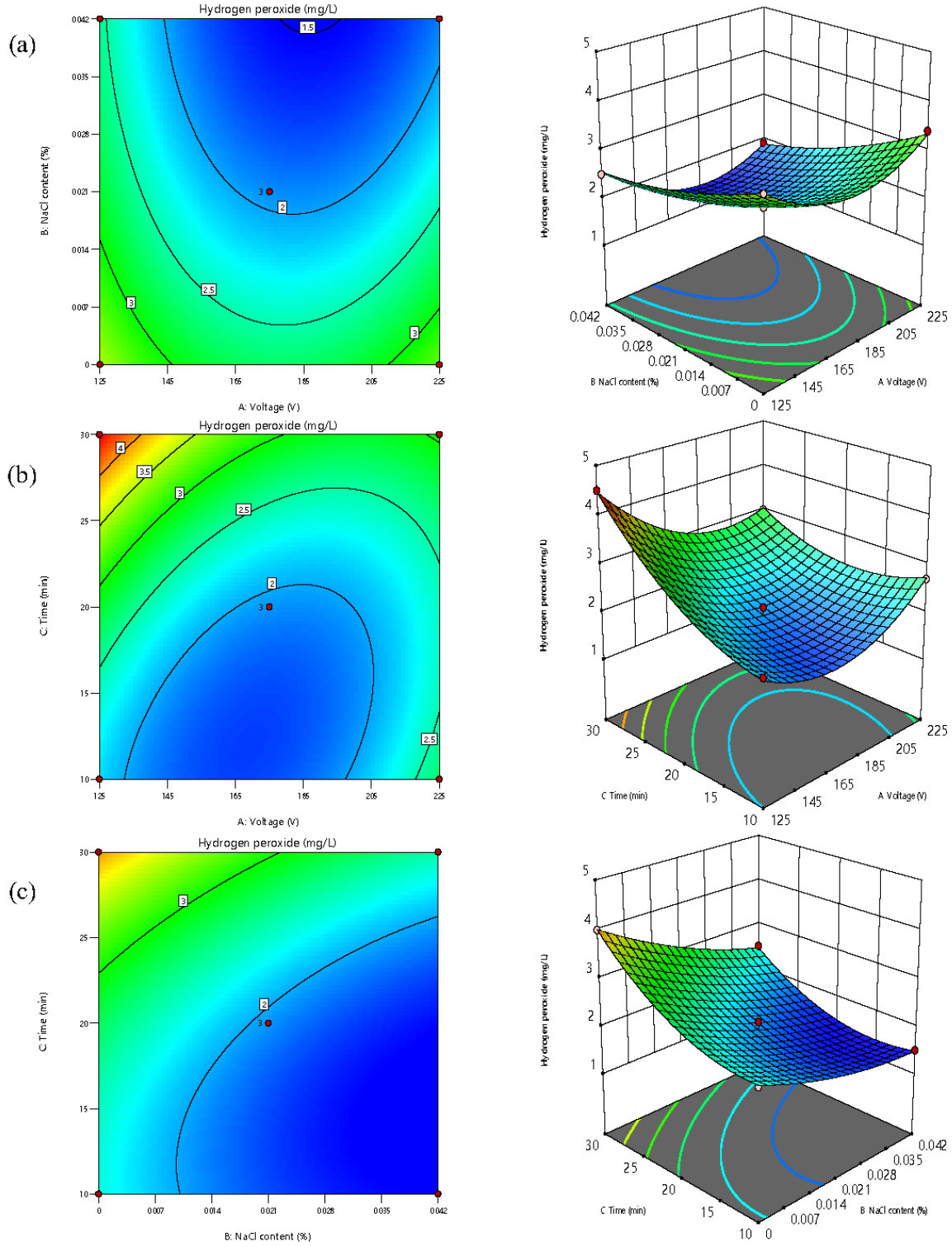


Figure 8

Interactive effects of input voltage, NaCl content, and treatment time on H_2O_2 concentration: (a) input voltage and NaCl content, (b) input voltage and treatment time, (c) NaCl content and treatment time.

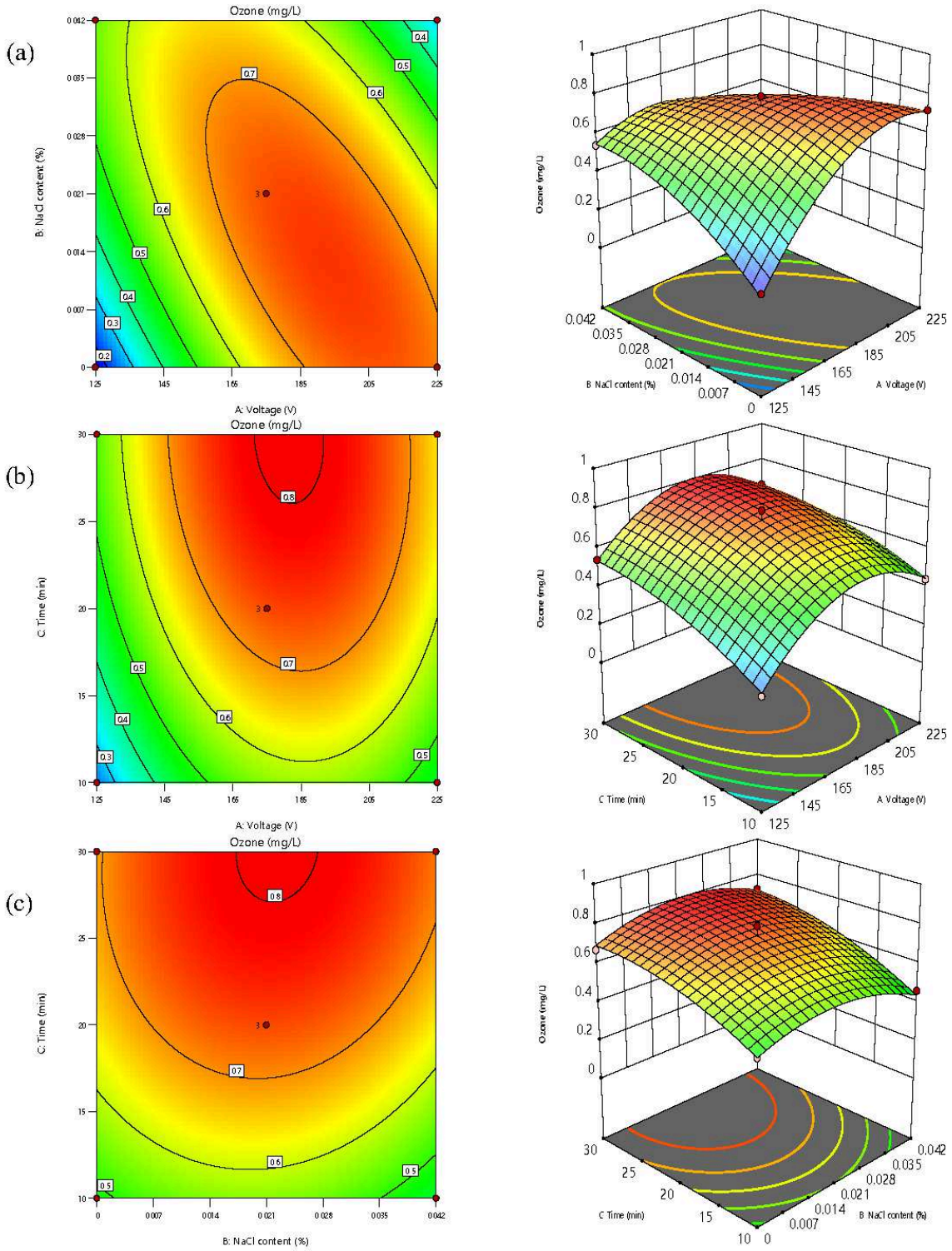


Figure 9

Interactive effects of input voltage, NaCl content, and treatment time on O_3 concentration: (a) input voltage and NaCl content, (b) input voltage and treatment time, (c) NaCl content and treatment time.

Supplementary Files

This is a list of supplementary files associated with this preprint. Click to download.

- 2025821Supplementarytable.docx
- 2025821tableschy.docx